10 Applied Science

10-1 Characterization of Nano-Textured AlN Thin Films Using X-Ray Absorption Near Edge Structure Spectroscopy

Thin films of wide-gap semiconductors are widely used in modern technology. In the present report, we demonstrate that the X-ray absorption near edge structure (XANES) technique is extremely useful when the crystal is too small or contains too many faults or strains to be analyzed using the conventional X-ray diffraction (XRD) technique.

Three different AlN thin films of 200 nm in thickness, obtained using the pulsed laser-deposition (PLD) technique, were studied. The details of the processing conditions are described elsewhere [1]. Figure 1 (a) shows XRD patterns of the three samples and a wurtzite-AlN (w-AlN) powder sample recorded using Cu-Kα radiation. Sample A shows only one reflection peak, which corresponds to the (0 0 0 2) reflection of the w-AlN crystal. Samples B and C do not show this reflection, but sample B exhibits a weak, broad reflection between 30° and 38° in the 2θ range that cannot be identified clearly.

Figure 1(d) shows experimental XANES spectra of sample A recorded at BL-11A using the total electron-yield (TEY) method. The sample was mounted with its surface orientated at 90° and 50° with respect to the incident X-ray beam. When measured with the 50°-geometry, the XANES spectrum of sample A is identical to that of the w-AlN powder. The angle used is close to $\cos^{-1}(1/\sqrt{3}) = 54.7°$, which should provide a XANES spectrum averaged over all crystallographic directions. When measured with the 90°-geometry, however, peaks B_2, C, and D_2 show a remarkable drop in intensity. Given the fact that sample A exhibits a high degree of texturing along the *c*-axis normal to the substrate, peaks B_2, C, and D_2 can be ascribed to the XANES components that appear only when measured with ***E*** parallel to *c*, where ***E*** is the electric field vector of the X-rays and *c* is the *c*-axis of the hexagonal crystal.

A first-principles orthogonalized-linear combination of atomic-orbitals (OLCAO) method was employed to calculate theoretical XANES spectra, which are shown in Fig. 1(c). In the calculations a core-hole was included in the Al-1*s* orbital and a 108-atom supercell was used. Computational details can be found in [2]. Figure 1(c) shows the theoretical XANES spectra for ***E*** perpendicular to *c*, ***E*** parallel to *c*, and for random conditions. The theoretical spectrum for w-AlN with random orientations satisfactorily reproduces the observed results for the w-AlN powder. An increase in intensity of peaks B_2, C, and D_2 is evident for ***E*** parallel to *c*, also in good agreement with the experimental spectra. We can therefore conclude that the absence of peaks B_2, C, and D_2 can be a good indication of a preferred orientation of *c* perpendicular to the film surface.

The experimental XANES spectra for the three samples with 90°-geometry and the crystalline w-AlN powder are displayed in Fig. 1(b). The spectrum of sample C is found to be very similar to that of the powder, implying that the local atomic environment and chemical bondings of the AlN in sample C, which was confirmed to be amorphous using XRD, should be very close to that of w-AlN. In other words, they should be randomly oriented. It is very interesting to note that the XANES spectrum of sample B resembles that of sample A, although no texturing of the crystals is evident from the XRD results for sample B. A careful inspection shows that the intensity ratio of the B_1 and A peaks is smaller in sample B, and that peak B_1 is broader in sample B.

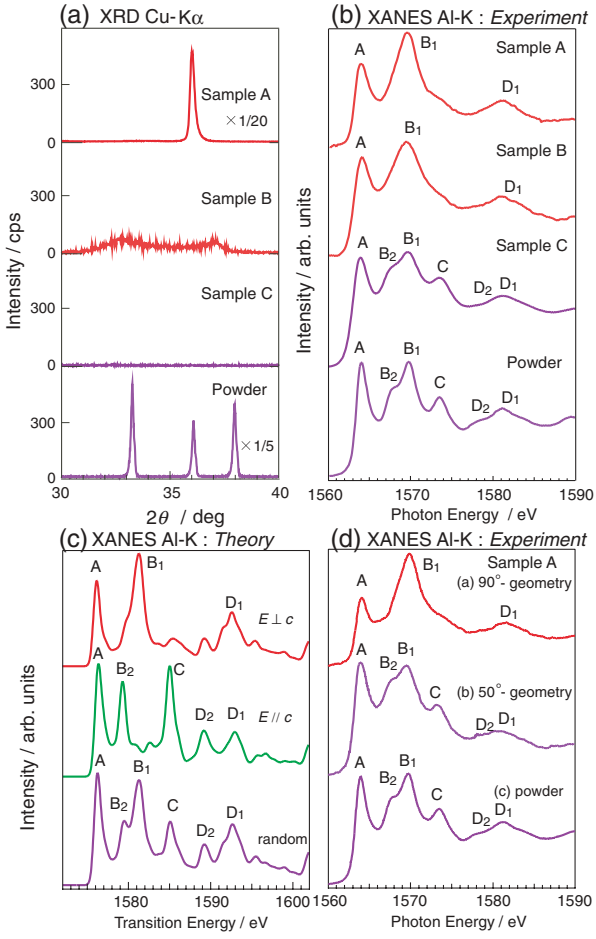

Figure 1
(a) Experimental XRD profiles (Cu-Kα), and (b) Al-K XANES spectra of the four AlN samples. (c) Theoretical Al-K XANES spectra with ***E***//*c*, ***E***⊥*c* and random conditions. (d) Experimental Al-K XANES spectra of sample A with two-geometries and of w-AlN powder.

The XANES spectrum of sample B should be most probably interpreted as indicating a nano-sized texturing of the AlN crystallites along the *c*-axis perpendicular to the substrate. The smaller relative intensity of peak B_1 suggests that the texturing is not as complete in sample B as it is in sample A.

I. Tanaka[1], T. Suga[1], S. Kameyama[1], S. Yoshioka[1], T. Yamamoto[2] and T. Mizoguchi[3] ([1]Kyoto Univ., [2]Waseda Univ., [3]The Univ. of Tokyo)

References

[1] T. Suga, S. Kameyama, S. Yoshioka, T. Yamamoto, I. Tanaka, and T. Mizoguchi, *Appl. Phys. Lett.*, **86** (2005) 163113.

[2] I. Tanaka, T. Mizoguchi and T. Yamamoto, *J. Am. Ceram. Soc.*, **88** (2005) 2013.

10-2 Crystal Structure of a New Phase in Metal-Doped Higher Fullerene $Rb_{8.8(7)}C_{84}$

Since the discovery of a superconducting phase in metal-doped C_{60} crystals, much effort has been devoted to a clarification of their crystal structures [1]. To date these studies have been confined to metal-doped C_{60} crystals since metal-doped crystals of the higher fullerenes have proved difficult to obtain. Recently, however, K-doped C_{84} crystals, $K_{8+x}C_{84}(D_{2d})$, $K_{8+x}C_{84}(D_2)$, $K_{3.5(1)}C_{84}(D_{2d})$ and $K_{2.6(1)}C_{84}(D_2)$, have successfully been synthesized and their crystal structures have been determined by Rietveld analyses of X-ray powder diffractions [2,3]. These studies suggested, furthermore, that $K_{3.5(1)}C_{84}(D_{2d})$ and $K_{2.6(1)}C_{84}(D_2)$ show metallic properties [3]. In the study described here, a new phase of Rb_xC_{84} has been prepared by the intercalation of Rb metal into C_{84} crystals, and the subsequent crystal structure was determined using X-ray powder diffraction.

The preparation of pure C_{84} samples is described elsewhere [4]. The preparation results in two isomers, $D_2(22)$-C_{84} and $D_{2d}(23)$-C_{84}, following the notation used in [5]. The molecular structures of $D_2(22)$-C_{84} and $D_{2d}(23)$-C_{84} are shown in Fig. 2. The Rb_xC_{84} sample was prepared by annealing a mixture of Rb metal and C_{84} in a glass tube at 623 K for 618 h. The X-ray diffraction pattern was recorded with synchrotron radiation at BL-1B, and Rietveld refinement was carried out using the Rietan 2000 program [6].

The X-ray diffraction patterns of Rb_xC_{84} at 6.5 and 295 K are shown in Figs. 3. All Bragg reflections can be indexed as a cubic lattice with *a* values of 16.82(2) Å at 6.5 K and 16.87(2) Å at 295 K. The *a* value at 295 K is larger than the corresponding values for K_xC_{84} (16.27 - 16.34 Å for $K_{\sim 3}C_{84}$, and 16.559 Å for $K_{\sim 8}C_{84}$) [2,3]. Consequently, this *a* of 16.87(2) Å is the largest value reported for the metal-doped fullerenes synthesized so far. The reflections observed in the X-ray diffraction patterns at 6.5 and 295 K indicate a space group $Pa\bar{3}$ for the crystals. This space group was also found in $M@C_{82}$ and C_{82} [7,8].

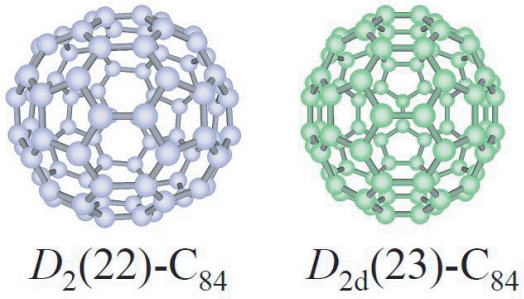

Figure 2
Molecular structures of $D_2(22)$- and $D_{2d}(23)$-C_{84}.

Only the molecular structure of $D_{2d}(23)$-C_{84} was used in the Rietveld refinement for Rb_xC_{84} because the current sample consists of more than 80% of $D_{2d}(23)$-C_{84}. The principal C_2 axis of D_{2d}-C_{84} extends along the [111] direction in the crystal lattice, and the D_{2d}-C_{84} molecule should be orientationally disordered around [111] to satisfy the space group $Pa\bar{3}$. The calculated pattern for Rb_xC_{84} at 6.5 K is also shown in Fig. 3(a). The final weighted pattern *R* factor, R_{wp}, and integrated intensity *R* factor, R_I, were 4.82% and 1.31%, respectively. The refined site occupancies of the Rb atoms were 74(3)%

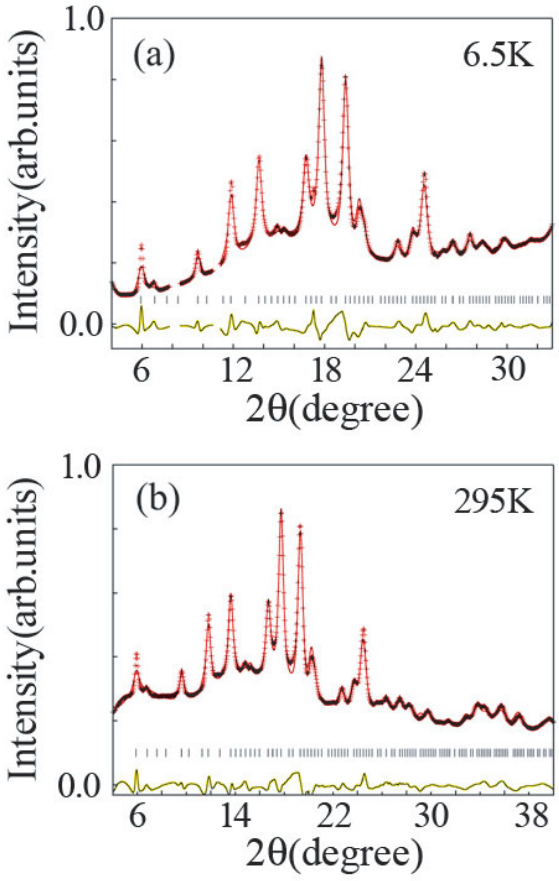

Figure 3
X-ray diffraction patterns calculated with the structural parameters determined by Rietveld refinement (solid red curves), and the observed patterns (black + symbols) at (a) 6.5 and (b) 295 K. Allowed peak positions are indicated with ticks, and the difference between the observed and calculated patterns are shown as solid yellow curves. The wavelength of X-ray beam was 1.0006 Å.

for the tetrahedral site (1/4,1/4,1/4), 17(5)% for the octahedral site (1/2,1/2,1/2), and 89(2)% for the (*x*,*x*,*x*) and (*x*,*x*,*1–x*) sites, showing that this phase is $Rb_{8.8(7)}C_{84}$. The value of *x* was 0.3866(3), where the (*x*,*x*,*x*) and (*x*,*x*,*1–x*) sites constitute the corners of the cubes around the octahedral sites. The shortest Rb-Rb distance in this cube is 3.82(1) Å, larger than the shortest K-K distance of 3.48(2) Å in $K_{3.5(1)}C_{84}$ [3]. The Rietveld refinement was performed for the X-ray diffraction pattern at 295 K based on the structure at 6.5 K, and the calculated pattern is shown in Fig. 3(b). The final values of R_{wp} and R_I were 3.66% and 1.73%, respectively.

In summary, a new phase of a metal-doped higher fullerene, $Rb_{8.8(7)}C_{84}$, has been successfully prepared. The crystal structure was determined by Rietveld analyses of X-ray powder diffraction data. The results of this study will open a way to develop and determine the structure of metal-doped higher fullerenes with novel physical properties.

Y. Kubozono and Y. Rikiishi (Okayama Univ., JST-CREST)

References

[1] Y. Iwasa and Y. Takenobu, *J. Phys.: Condens. Matter,* **15** (2003) R495.

[2] K. M. Allen, T. J. S. Dennis, M. J. Rosseinsky and H. Shinohara, *J. Am. Chem. Soc.*, **120** 6681 (1998).

[3] M. S. Denning, T. J. S. Dennis, M. J. Rosseinsky and H. Shinohara, *Chem. Mater.*, **13** 4753 (2001).

[4] Y. Rikiishi, Y. Kashino, H. Kusai, Y. Takabayashi, E. Kuwahara, Y. Kubozono, T. Kambe, T. Takenobu, Y. Iwasa, N. Mizorogi, S. Nagase and S. Okada, *Phys. Rev. B,* **71** (2005) 224118.

[5] P. W. Fowler and D. E. Manolopoulos, *An Atlas of Fullerenes*. (Clarendon, Oxford, 1995).

[6] F. Izumi, in *The Rietveld Method*, edited by R. A. Young (Oxford University Press, Oxford) (1993) 236.

[7] Y. Kubozono, Y. Takabayashi, K. Shibata, T. Kanbara, S. Fujiki, S. Kashino, A. Fujiwara and S. Emura, *Phys. Rev. B,* **67** (2003) 115410.

[8] Y. Kubozono, Y. Rikiishi, K. Shibata, T. Hosokawa, S. Fujiki and H. Kitagawa, *Phys. Rev. B*, **69** (2004) 165412.

10-3 Resonant X-Ray Emission Spectroscopy Study of (Ga,Mn)As

Diluted magnetic semiconductors (DMS) formed by doping magnetic ions into a semiconductor host have attracted much attention due to the coexistence of electronic and magnetic functionalities [1]. For the III-V based DMS (Ga,Mn)As, the Mn impurities induce magnetic moments and carriers (holes), leading to ferromagnetism due to Mn-Mn interaction via the carriers. This carrier-induced ferromagnetism, which can be controlled by external parameters such as light illumination [2] or electric fields [3], is especially important from the viewpoint of applications to devices, and the driving mechanism has been frequently discussed. In order to understand carrier-induced ferromagnetism, it is essential to clarify whether the holes mediating the ferromagnetism are bound to Mn acceptors (neutral acceptor states; A^0) or activated (ionized acceptor states; A^-). The local electronic structure around the Mn ions can be observed under core excitation with synchrotron radiation. In this study, we have performed high-resolution Mn L_3 ($2p_{3/2}$) resonant X-ray emission spectroscopy (RXES) of (Ga,Mn)As at BL-2C. RXES is an experimental technique that probes the emitted photon energy (ω) of X-rays following the excitation of a core electron near the absorption threshold [4]. Metal 2*p*-3*d*-2*p* RXES is a second-order (coherent absorption and emission of photons) optical process, with *d*-*d* transitions allowed depending on the valency of the magnetic ion. For Mn 2*p* RXES in (Ga,Mn)As, it should be possible to resolve clearly the features of the A^0 (Mn^{3+} or Mn^{2+} with a bound hole) state and the A^- (Mn^{2+}) state. Furthermore, the resonance effect should enhance either the A^0 or A^- state by tuning the incident-photon energy Ω to each of the absorption features, which are separated by the chemical shift. Hence RXES is an important tool for characterizing the Mn acceptor state in (Ga,Mn)As.

Figure 4 shows the RXES spectra plotted as a function of energy loss ω-Ω for (Ga,Mn)As (Mn content *x*

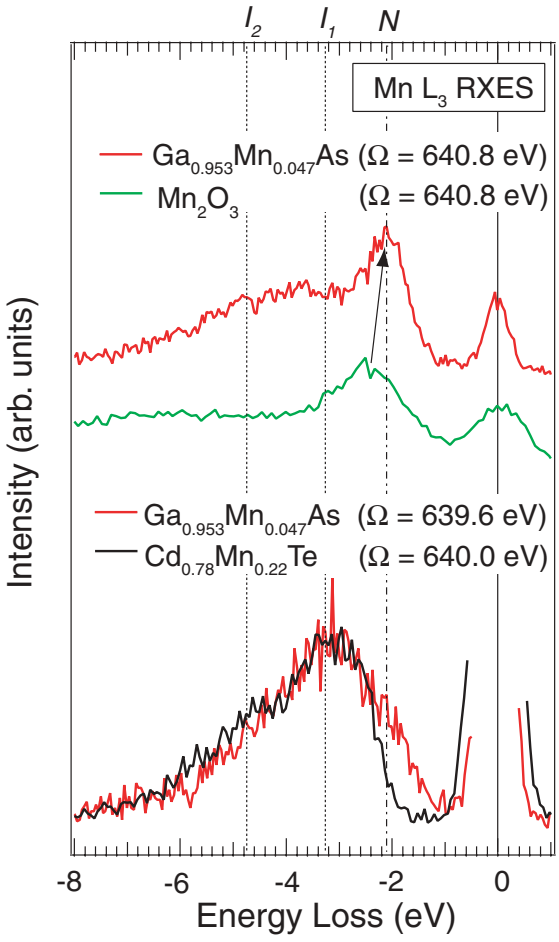

Figure 4
Comparison of RXES spectra in the Mn L_3 region: (i) (Ga,Mn)As excited at 639.6 eV (red-curve) and (Cd,Mn)Te excited at 640.0 eV (black-curve spectrum) and (ii) (Ga,Mn)As excited at 640.8 eV (red-curve) and Mn_2O_3 excited at 640.8 eV (green-curve).

= 0.047) (red curve), II-VI-based DMS (Cd,Mn)Te (x = 0.22) (black curve) and Mn_2O_3 (green curve) in the Mn L_3 absorption region at room temperature. (Cd,Mn)Te and Mn_2O_3 are used as references for the A^- and A^0 signals, respectively. The *d-d* transitions in the (Ga,Mn)As spectra are divided into two groups labelled $I_{1,2}$ (dotted curve) and N (dash-dot curve). The enhancement of $I_{1,2}$ occurs at Ω = 639.6 eV, corresponding to an incident photon energy at the L_3 absorption peak (not shown) [5], while that of N occurs at Ω = 640.8 eV above the L_3 resonance. The (Cd,Mn)Te spectrum, obtained with Ω corresponding to the photon energy at the L_3 absorption peak (not shown) [5], well reproduces $I_{1,2}$ and shows no clear feature about N. On the other hand, the Mn_2O_3 spectrum excited at 640.8 eV shows a feature near N. It is known that the lowest *d-d* excitation in Mn^{3+} ions is lower in energy than that in Mn^{2+} ions . Furthermore, the difference between Ω = 639.6 eV and 640.8 eV, corresponding to the resonances at $I_{1,2}$ and N, is comparable to the chemical shift between the Mn^{2+} and Mn^{3+} states, taking into account screening for the A^- components. Therefore, it can be concluded that $I_{1,2}$ and N are attributable to the A^- and A^0 signals of (Ga,Mn)As. The coexistence of A^- and A^0 states suggests that the ferromagnetic coupling could be attributed to the double-exchange-like interaction as well as to the free-carrier-induced interaction.

Y. Ishiwata[1] and S. Shin[2] ([1]Saga Univ., [2]The Univ. of Tokyo, ; RIKEN/Spring-8)

References

[1] H. Ohno, *Science*, **281** (1998) 951.
[2] S. Koshihara, A. Oiwa, M. Hirasawa, S. Katsumoto, Y. Iye, C. Urano, H. Takagi, H. Munekata, *Phys. Rev. Lett.*, **78** (1997) 4617.
[3] H. Ohno, D. Chiba, F. Matsukura, T. Omiya, E. Abe, T. Dietl Y. Ohno and K. Ohtani, *Nature,* **408** (2000) 944.
[4] A. Kotani and S. Shin, *Rev. Mod. Phys.*, **73** (2001) 203.
[5] Y. Ishiwata, T. Takeuchi, R. Eguchi, M. Watanabe, Y. Harada, K. Kanai, A. Chainani, M. Taguchi, S. Shin, M. C. Debnath, I. Souma, Y. Oka, T. Hayashi, Y. Hashimoto, S. Katsumoto and Y. Iye, *Phys. Rev. B*, **71** (2005) 121202(R).

10-4 Positron Transmission Images

Introduction

A positron is the anti-particle of an electron. Positrons are quite useful for studying Fermi surfaces, defects and phase transitions in materials. Normally the speed of positrons produced either via nuclear decays or by accelerators covers a wide range of values (a "white" distribution). It is possible to use a modulator substance to decelerate a beam of positrons to kinetic energies of the order of kT. Slow positrons are ejected from the surface of the substances which has a negative work function of the order of 1 eV. The positrons can be accelerated to the desired speed. When a positron beam having a particular energy is focused, the properties within the fine beam can be studied.

X-ray transmission photography has been widely used for more than one hundred years. Similar photographs obtained using positrons should be useful not only for the study of properties of positrons, but also for studying unprecedented positron visual images of defect structures and structural changes concomitant with phase transitions in solids. In this paper, such a visualization of transmission positron images is presented using imaging plates with a positional resolution of a few tens of micrometers. Transmission pictures obtained with positrons are sometimes different from those obtained with X-rays or electrons, since positrons can be captured by vacancies, open volumes and internal structures within the specimen, whereas X-rays and electrons can not. In some cases, images with higher contrast can be obtained using positrons. It has proved difficult to obtain uniform positron beams with diameters of around 0.1 mm, but by this method the distribution of intensity can be measured. The energies (speeds) of positrons suitable for obtaining transmission positron images can be selected to be either discrete or continuous (white). Images with positrons can be recorded in vacuum, in air or in any atmosphere, as is the case for X-rays. The images can be recorded on photographic films, imaging plates, fluorescent plates, channel plates, multi-wire proportional counters, or by a combination of them. A wide range of future applications can be expected. Imaging plates are highly sensitive to positrons [1], and no complex equipment is needed. Specimens can be mounted in daylight, but darkness is required during exposure for the imaging plates. The resultant images can be erased by UV light irradiation, allowing the plates to be re-used. In this report, applications of imaging plates to transmission images are presented. Another advantage of this technique is that sealed positron emitters such as ^{22}Na can be used, removing the need for special radioactive isotope permissions in most countries. The ^{22}Na source has a long half-life time of 2.6 years, making it be a convenient source for imaging applications. Positrons penetrate deeper into materials than electrons. This is because positrons are positively charged and are thus repelled by the ions and atoms within specimens and can pass through interstitial spaces, in contrast to electrons which are attracted by atoms and collide with electrons and nuclei.

The slow positron facility at KEK was used for fixed positron energy experiments. The facility [2] consists of a 50-MeV electron LINAC, and an assembly consisting of a slow positron generator, a low-energy positron transport line and an experimental station for positronium time-of-flight (Ps-TOF) spectroscopy. In a water-cooled tantalum target 2 mm thick, energetic electrons from the LINAC produce bremsstrahlung photons, leading to the pair creation of electrons and positrons. The resulting energetic positrons are slowed down as

they pass through seven 25-μm-thick tungsten-sheet converters which have been annealed at 2273 K under an ultrahigh vacuum. The assembly has a Wehnelt with photo-chemically manufactured grid used to extract slow positrons. The kinetic energy of the positrons can be varied over a range 1 keV to 35 keV. The flux intensity of energy-selected positrons is about 10^6 e^+/s.

Imaging plates

Imaging Plates BAS-TR2025 for the bio imaging analyzer BAS2500 or Imaging Plates for digital micro-luminography (Type FDL UR-V) were used. Photo-stimulated luminescence (PSL) usually has a very wide dynamic range. The logarithm of the detected number of photo-stimulated-luminescence photons is taken to shrink the imaging data to a narrower range. The number is then quantized and rounded to an integer. This value is called the QL (Quantum Level). The output of the "IPReader", the commercial name of an imaging plate reader, is maintained in the QL form. The grade of the number of positrons detected at each pixel can be recorded as 8 bits (Grad 256), 10 bits (Grad 1024), or 16 bits (Grad 65536). A grade of 16 bits was selected for this experiment. PSL is proportional to the number of photo-stimulated-luminescence photons. The photo-stimulated luminescence per area, *I*, can be represented as PSL/mm^2. The relation between PSL and QL is defined as [3]

$$PSL = (Pixel\ Size/100)^2 \times (4000/Sensitivity) \times 10^{**}(Latitude-(QL/Grad - 0.5)),$$

PSL = 0, when QL = 0 where Grad = 2^{**}bit.

For the same kind of particles, the reading density is the same. Hence comparison between different exposures is possible. Here we have used sensitivity = 4000, latitude = 5, and Grad = 1024.

The PSL is proportional to the fluence of positrons over a range of 1 to one million [1]. This behaviour is much more sensitive and quantitative than that of photographic films, making imaging plates very convenient for recording positron images.

Comparison of images obtained using mono-energetic positrons and electrons

The BAS-TR2025 imaging plates were cut into a size of 30 mm x 30 mm. These imaging plates do not have protective layers to respond to slow positron or electron beams. The Imaging Analyzer BA2500 at Photon Factory was used to analyze the positron and electron images recorded on the imaging plates. We chose a pixel size of 50 μm x 50 μm. This was the smallest available size for the Imaging Analyzer BA2500.

Figure 5 (a) shows a transmission image of a dorsal fin generated using 40-keV electrons and Fig. 5(b) is an image of the same specimen obtained using 30-keV positrons.

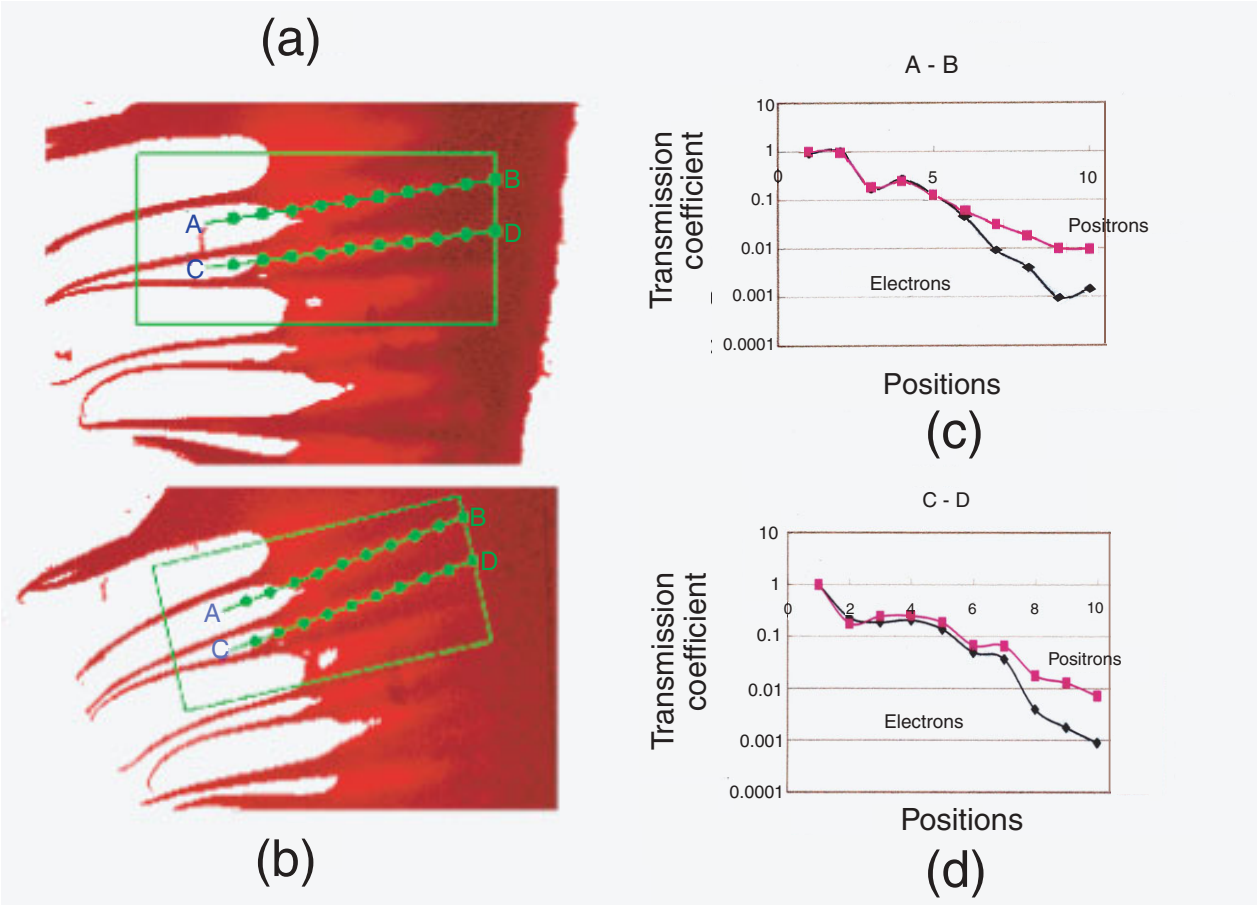

Figure 5
Comparison of images obtained using (a) 40-keV electrons and (b) 30-keV positrons. Penetration of electrons and positrons along (c) the AB line and (d) the CD line shown in (a) and (b).

As shown in Figs. 5(c) and (d), the transmission coefficients for 40-keV electrons and 30-keV positrons are nearly the same over a position range index of 1 to 6. This implies that while the energies of positrons and electrons are high, the transmission difference between positrons and electrons is not large, but when the energies of positrons and electrons are low the difference is large.

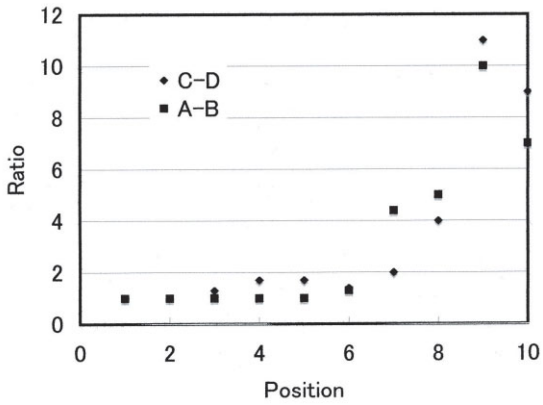

Figure 6
Ratio (shown in the text) vs. positions.

We define here a ratio as

$$\text{Ratio} = (\mu_{e+}/m_{e-})_0/(\mu_{e+}/m_{e-})_i \quad ,$$

where μ is the transmission coefficient, and subscripts 0 and i stand for the incident beam and position index, respectively. Although the thickness was not measured, it becomes thicker as the position index number is increased.

The result of Fig. 6 shows that the ratio is monotonically increased as the position number is higher. This shows that positrons with low energies penetrate deeper into materials than electrons with the same energy.

M. Doyama[1], Y. Kogure[1], M. Inoue[1] and T. Kurihara[2]
([1]Teikyo Univ. [2]KEK-PF)

References

[1] M. Doyama, M. Inoue, T. Yoshiie, Y. Hayashi, M. Kiritani and T. Oikawa, *Nucl. Instrum. Meth. Phys. Res. A*, **448** (2000) 554.
[2] M. Doyama, Y. Kogure M. Inoue Y. Hayashi, T. Yoshiie, T. Kurihara, R. Oshima and K. Tsuno, *Mater. Sci. Forum* **445** (2004) 471.